J. Fluid Mech. (2025), *vol.* 1025, A46, doi:10.1017/jfm.2025.10975

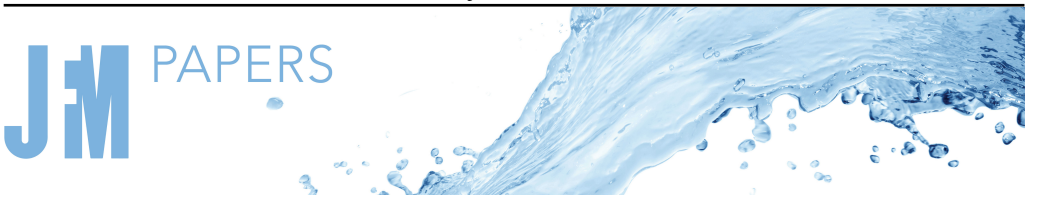

Growth of reattachment streaks in hypersonic compression-ramp flow

Henry Broadley[1] **and Richard Hewitt**[2]

[1]School of Engineering, The University of Manchester, Manchester M13 9PL England, UK

[2]Department of Mathematics, The University of Manchester, Manchester M13 9PL, England, UK

Corresponding author: Henry Broadley, henry.broadley@manchester.ac.uk

(Received 9 June 2025; revised 10 October 2025; accepted 16 November 2025)

Both experiments and direct numerical simulation (DNS) of hypersonic flow over a compression ramp show streamwise aligned streaks/vortices near the corner as the ramp angle is increased. The origin of this three-dimensional disturbance growth is not definitively known in the existing literature, but is typically connected to flow deceleration, centrifugal (Görtler) and/or baroclinic effects. In this work we consider the hypersonic problem with moderate wall cooling in the high Reynolds/Mach number, weak interaction limit. In the lower deck of the corresponding asymptotic triple-deck description we pose the linearised, three-dimensional, Görtler stability equations. This formulation allows computation of both receptivity and biglobal stability problems for linear spanwise-periodic disturbances with a spanwise wavelength of the same order as the lower-deck depth. In this framework the dominant response near the ramp surface is of constant density and temperature (at leading order) ruling out baroclinic mechanisms. Nevertheless, we show that there remains strong energy growth of upstream spanwise-varying perturbations and ultimately a bifurcation from two-dimensional to three-dimensional ramp flow. The unstable eigenmodes are localised to the separation region. The bifurcation points are obtained over a range of ramp angle, wall-cooling parameter and disturbance wavelength. Consistent with DNS results, the three-dimensional perturbations in this asymptotic formulation are streamwise aligned streaks/vortices, displaced above the separation region. In addition, the growth of upstream disturbances peaks near to the reattachment point, whilst the streaks persist beyond it, decaying relatively slowly downstream along the deflected ramp.

Key words: boundary layer stability, hypersonic flow

1. Introduction

The supersonic/hypersonic compression ramp is a common test bed problem in the investigation of high-speed flow separation, instability, transition and heat transfer. It is a configuration that has to date been explored by a combination of experimental (Simeonides & Haase 1995), numerical (direct numerical simulation (DNS)) (Navarro-Martinez & Tutty 2005) and asymptotic (high Reynolds/Mach numbers) methods (Brown, Cheng & Lee 1990; Cassel, Ruban & Walker 1996). With increased computational resources, DNS results in particular have progressed substantially in recent years revealing the importance of three-dimensional instabilities of separated flow in the vicinity of the compression ramp 'corner', however, the physical origin of these three-dimensional effects are still being addressed in the literature; (see Sidarth *et al.* 2017; Dwivedi *et al.* 2019 and Hao *et al.* 2021) for example. Whatever the precise details of the generation mechanism are, the manifestation of this three-dimensionality is typically an array of streamwise-aligned steady streaks/vortices that dominate in the reattachment part of the flow (downstream of the ramp corner). At sufficiently large flow speed and ramp angle, the resulting nonlinear streaks are thought to become unstable to wave-like perturbations, providing a route to turbulence and an increased heat transfer.

Our focus in this work will be the planar compression ramp formed by an impermeable boundary with zero incidence to a uniform high-speed flow. At some distance L from the leading edge, this flat boundary is deflected by an angle θ to the oncoming stream to yield a concave ramp flow. At a critical deflection angle, the two-dimensional planar flow separates near the corner, and as the angle is increased the separation and reattachment points move upstream and downstream, respectively. In both experimental and DNS results, this separated flow typically becomes spanwise varying and there are low frequency unsteady effects that can appear, including weak oscillation of the separated region. Most relevant to our current discussion are the above-mentioned streaks.

Early experimental/DNS results, for example Simeonides & Haase (1995) and Navarro-Martinez & Tutty (2005), pointed to the appearance of spanwise varying heat transfer rates at the ramp surface when a small, steady spanwise periodic disturbance was introduced upstream of the separation region. In one case Navarro-Martinez & Tutty (2005) also noticed the spontaneous appearance of downstream striations even in the absence of explicit upstream forcing. It was suggested that the underlying mechanism generating the three-dimensional response was centrifugal in nature, owing to curvature of the flow over the ramp. Early efforts were made to approximate a Görtler number for these flows by estimating the curvature. This involved a simple geometric argument, fitting a circle through separation/reattachment points that was tangent to both flat/inclined boundaries by Grasso & Marini (1995), whilst the Navarro-Martinez & Tutty (2005) work modified this slightly to require the circle to be tangent to the undeflected boundary, rather than also explicitly through the separation point. Their conclusion was that the Görtler mechanism plausibly explained growth of three-dimensional disturbances in these flows, but the argument was inevitably somewhat qualitative. Previously, the work of Inger (1977) had also emphasised the possible role of centrifugal instability and growth of Görtler-type vortices driven by curvature near a separation line, see also Xu, Ricco & Duan (2024). Subsequently this approach has been applied to boundaries of constant curvature by Uy, Hao & Wen (2023), whilst a more detailed computation of a Görtler number from the numerical data in ramp flows was undertaken by Cao, Klioutchnikov & Olivier (2019). Later experimental results can be found in (for example) Chuvakhov *et al.* (2017).

More recently, Sidarth *et al.* (2017, 2018) computed eigenmodes of the linear global stability problem via the compressible Navier–Stokes equations (NSE) to reveal global modes that dominate within the separation bubble. A similar global stability approach was taken by Hao *et al.* (2021) where again eigenmodes were found local to the separation region, furthermore an energy budget analysis showed production (their figure 13) was localised to the eye of the primary vortex within the separated zone. Their results also linked the appearance of this global instability to secondary separation in the corner.

Dwivedi *et al.* (2019) explored the development of upstream disturbances in the hypersonic compression ramp via DNS coupled to an input–output analysis including both steady and unsteady perturbations. They examined ramp inclinations for which there are no unstable global modes, to allow a focus on the growth of externally imposed upstream disturbances. Their comprehensive results showed that downstream streaks developed from upstream (counter rotating) vortical perturbations with strong amplification of low-frequency perturbations. In addition, for steady streaks their results highlighted that particularly in cold-wall flows, baroclinic effects dominate the growth in contrast to the previous discussions that concentrated on streamline curvature.

We now turn to theoretical/asymptotic methods provided by the triple-deck model, e.g. Neiland (1969) and Stewartson & Williams (1969) amongst others. This modification to boundary-layer theory allowed for inclusion of upstream influence, and was applied to three-dimensional flows by Smith (1976*a*,*b*). The triple-deck structure has also been applied to instabilities, for example in incompressible flow (Smith 1979*a*; Smith 1979*b*), supersonic/hypersonic flow (Smith 1989) and the receptivity of boundary-layers (Terent'ev 1981). The planar compression ramp has a long history of examination in this large Reynolds number ($Re \gg 1$) limit and the work of Ruban (1978), Rizzetta, Burggraf & Jensen (1979), Smith & Khorrami (1991) or Korolev, Gajjar & Ruban (2002) all provide results for separated states over increasing ranges of ramp angles. The formulation in these cases was for free stream Mach numbers $M_\infty = O(1)$ and ramp angles that are of $O(Re^{-1/4})$. This regime results in a canonical triple-deck formulation, with the lower deck and interaction condition providing a nonlinear system that captures the separated flow in a streamwise region within $O(Re^{-3/8})$ of the ramp 'corner'.

There are a number of authors that have considered the two-dimensional instability of these solutions within the context of the triple-deck description, such as Cassel, Ruban & Walker (1995), Fletcher, Ruban & Walker (2004), Logue, Gajjar & Ruban (2014) and most recently Broadley, Hewitt & Gajjar (2023). The prospect of three-dimensional instability of these triple-deck ramp states has received little attention. It is important to note that in the triple-deck formalism, the lower deck problem spans a $O(Re^{-5/8})$ region adjacent to the boundary, which remains thin compared with the $O(Re^{-1/2})$ boundary layer impinging on the corner region at the base of the ramp. A consequence of this is that the flow in the lower deck is effectively incompressible at leading order, with a constant temperature and density corresponding to the wall values of the impinging boundary layer. This raises some obvious questions in the above-described debate regarding centrifugal versus baroclinic mechanisms for the growth of reattachment streaks in compression ramp flows, since clearly any vortex/streak structure that can be accommodated in this leading-order lower-deck problem must necessarily not have a baroclinic growth mechanism. Our goal in this work is to therefore investigate the behaviour of spanwise varying perturbations using the $Re \gg 1$ triple deck description.

Moving from a $M_\infty = O(1)$ to a hypersonic ($M_\infty \gg 1$) regime with wall cooling effects requires some modifications to the triple-deck structure; we describe these in more detail in the following section. The first formulation was provided by Neiland (1973) for flow near a separation point occurring on a flat plate. The corresponding ramp geometry was first

considered by Brown *et al.* (1990), though the details of their formulation of the interaction problem differ slightly from Neiland (1973), with the latter approach being followed in the subsequent work of Kerimbekov, Ruban & Walker (1994) and Cassel *et al.* (1996). A discussion of the differences between the two formulations can be found in the appendix of Cassel *et al.* (1996). In either approach the upstream boundary-layer must now be split into two distinct regions as the wall cooling occurs in a thin layer. The interaction problem is similarly modified to contain two parts, firstly there is the familiar displacement associated with the viscous lower deck but in addition a new term arises from a displacement effect in the main deck. In the regime we will examine, the lower deck remains thin compared with the upstream cooled wall layer and compressibility effects still do not directly enter into the description. As a result, the canonical hypersonic problem in terms of the lower deck variables only differs from the supersonic case by way of an extra term in the interaction condition; this condition becomes (2.8) below.

In what follows we will first formulate a wall-cooled hypersonic triple-deck description to study the stability of the two-dimensional base states to three-dimensional disturbances. A set of linear disturbance equations in the lower deck will be formulated in the manner of Hall & Bennett (1986); this approach describes a bidirectional parabolic system for the evolution of perturbations of Görtler type. We assume that the spanwise wavelength of the instability is comparable to the lower deck transverse scale; or equivalently the order of magnitude of the separating streamline from the ramp surface. We solve the linear steady disturbance equations subject to steady perturbations introduced upstream ahead of separation, and compute the downstream growth as the disturbance progresses through the separated flow. The results will span a range of ramp angles to demonstrate the existence of Görtler instabilities, before we turn our attention to the possibility of global (temporal) instabilities, by solving both an initial-value problem and comparing with a biglobal eigenvalue analysis.

2. Governing equations

For an asymptotic formulation we take the Reynolds/Mach numbers to be large (see for example Ruban (2017) § 1.11.2) where

$$Re = \frac{\rho_\infty U_\infty L}{\mu_*}, \quad M_\infty = U_\infty \left(\frac{\gamma p_\infty}{\rho_\infty}\right)^{-1/2}, \tag{2.1}$$

in addition we will assume that the problem can be described in the weak hypersonic interaction regime, with

$$\chi = M_\infty^2 Re^{-1/2} \ll 1, \tag{2.2}$$

and ignore real gas effects. Here U_∞, p_∞, ρ_∞ are the free stream values of the velocity, pressure and density, L is the leading-edge to ramp distance and γ is the specific heat ratio (assumed constant). Note that for strong interaction ($\chi = O(1)$ or even larger) the triple-deck structure is not applicable (see Brown *et al.* (1990) for details).

The problem is made dimensionless using L, U_∞, p_∞, ρ_∞ in the usual manner, with the enthalpy

$$h = U_\infty^2 \hat{h}\,. \tag{2.3}$$

The viscosity is then assumed to be

$$\mu = \mu_* \hat{h}^n, \tag{2.4}$$

where n is a positive constant; leaving μ_* as the viscosity at the reference enthalpy U_∞^2.

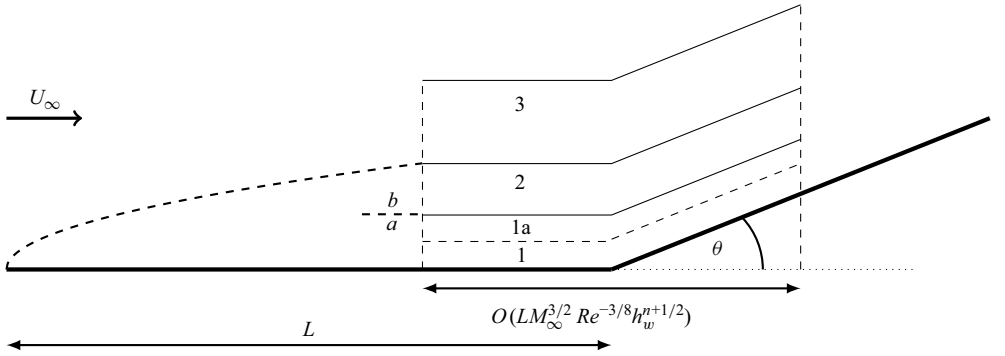

Figure 1. A schematic of the triple-deck regions. The ramp is a distance L from the leading edge and the triple-deck formulation spans a downstream scale of $O(LM_\infty^{3/2}Re^{-3/8}h_w^{n+1/2})$ around this point. The ramp angle θ for which this interaction develops is $O(Re^{-1/4})$. Ahead of the ramp region, under wall cooling the upstream boundary layer consists of two layers here denoted by a and b.

Upstream of the triple-deck region the bulk of the impinging boundary layer has a (dimensionless) thickness of $O(M_\infty Re^{-1/2})$ and a low density $O(M_\infty^{-2})$; this is the region denoted by b in the schematic of figure 1. However, when the wall is cooled sufficiently, such that the dimensionless enthalpy evaluated on the boundary is $\hat{h}_w = h_w/U_\infty^2 \ll 1$ this upstream layer divides into two, with a thinner near-wall region of thickness $O(M_\infty Re^{-1/2}\hat{h}_w^{n+1})$. This thin region is denoted by a in figure 1, and here the density increases to $O(M_\infty^{-2}\hat{h}_w^{-1})$ as the flow accommodates the cooled state of the wall. This parameter is equivalent to $\hat{h}_w = T_w/2T_0$ where T_0 is the stagnation temperature.

As shown in figure 1 the thin cooled region a is thick compared with the lower viscous deck 1, and its influence continues into the asymptotic corner description as region $1a$. Therefore, the solution in the lower deck 1 only depends on the upstream flow solution in a through its properties evaluated on the wall. This gives a largely standard viscous, nonlinear triple-deck problem, with a constant density and viscosity, as in the simpler supersonic case, with the addition of a term in the interaction condition that amounts to a contribution from region 2 (figure 1) due to wall cooling.

2.1. *Steady, two-dimensional base flows*

We begin by considering steady (two-dimensional) solutions to the lower deck at the base of the ramp. This problem is described by the triple-deck formulation, with further details outlined by Kerimbekov *et al.* (1994) or Cassel *et al.* (1996). For dimensionless coordinates $(\hat{x}, \hat{y})$, this lower layer is defined in terms of the new scaled coordinates

$$\hat{x} = 1 + M_\infty^{3/2}Re^{-3/8}\hat{h}_w^{n+1/2}\,X, \tag{2.5a}$$

$$\hat{y} = M_\infty^{3/2}Re^{-5/8}\hat{h}_w^{n+1/2}\,Y, \tag{2.5b}$$

where, the dimensionless variables are now expanded as

$$(\hat{u}, \hat{v}) = M_\infty^{1/2}Re^{-1/8}\hat{h}_w^{1/2}\big(\lambda Y + U_B(X, Y), Re^{-2/8}V_B(X, Y)\big), \tag{2.5c}$$

$$\hat{p} = 1 + \gamma M_\infty Re^{-2/8}P_B(X) + \cdots, \tag{2.5d}$$

$$\hat{h} = \hat{h}_w + \cdots, \tag{2.5e}$$

$$\hat{\rho} = \frac{1}{\gamma - 1}\frac{1}{M_\infty^2 \hat{h}_w} + \cdots. \tag{2.5f}$$

The value of λ depends on the (shear of the) upstream boundary layer a (figure 1) impinging on the ramp.

In this thin layer adjacent to the ramp surface the problem is effectively one of constant enthalpy and therefore constant density, viscosity, temperature – a spatially varying correction to the enthalpy (for example) will only develop at a higher order of $O(Re^{-1/4} M_\infty \hat{h}_w)$. The resulting equations contain the parameters λ, γ and the ramp angle α (where $\theta \sim \alpha Re^{-1/4}$ in figure 1); however, they can be rescaled to remove any explicit dependence on λ and γ. Applying this transformation and a Prandtl transform to a coordinate system measured relative to the ramp surface, we reduce the lower deck to a canonical form

$$(U_B + Y)\frac{\partial U_B}{\partial X} + V_B\left(1 + \frac{\partial U_B}{\partial Y}\right) = -\frac{\mathrm{d}P_B}{\mathrm{d}X} + \frac{\partial^2 U_B}{\partial Y^2}, \tag{2.6a}$$

$$\frac{\partial U_B}{\partial X} + \frac{\partial V_B}{\partial Y} = 0, \tag{2.6b}$$

subject to the boundary conditions

$$U_B = V_B = 0, \quad \text{at} \quad Y = 0, \tag{2.7a}$$

$$U_B,\, V_B,\, P_B,\, A_B \to 0, \quad \text{as} \quad X \to -\infty, \tag{2.7b}$$

$$U_B \to A_B + \alpha F, \quad \text{as} \quad Y \to \infty, \tag{2.7c}$$

as well as the interaction condition for hypersonic flow

$$P_B = -\frac{\mathrm{d}A_B}{\mathrm{d}X} + S\mathscr{L}\frac{\mathrm{d}P_B}{\mathrm{d}X}, \tag{2.8}$$

where A_B is the usual triple-deck displacement function. The wall cooling only appears through the last term in this interaction condition (Kerimbekov *et al.* 1994). The parameters S, $\mathscr{L}$ are defined through

$$S = M_\infty^{1/2} \hat{h}_w^{-n-1/2} Re^{-1/8}, \quad \mathscr{L} = \int_0^\delta \left(\frac{1}{M(Y)^2} - 1\right) \mathrm{d}Y \tag{2.9}$$

where δ is the boundary-layer thickness impinging on the ramp corner and M is the local leading-order Mach number distribution immediately upstream of the interaction region. While $S > 0$, $\mathscr{L}$ may be positive or negative, however, our focus will be on the 'supercritical' regime with an average upstream Mach number greater than unity, leading to $\mathscr{L} < 0$.

In the case $S|\mathscr{L}| \ll 1$ this problem reduces to the supersonic triple deck, where the wall temperature is not sufficient to affect the computational problem but the value of the wall temperature will still affect the rescaling of the computational solution via (2.5). However, if the wall is cooled sufficiently for $S\mathscr{L} = O(1)$ then the the computation becomes directly dependent on the wall temperature and the details of the impinging flow via (2.8)–(2.9), in addition to the ramp angle α.

We choose the ramp shape to be the smooth version proposed by Smith & Khorrami (1991) for the supersonic case,

$$F(X) = \frac{X}{1 + e^{-qX}}, \tag{2.10}$$

where q is a positive constant and throughout this study we use $q = 4$. The role of more gradual transitions to the inclined surface can be found in the DNS results of Cao *et al.* (2023) where an arc of a circle parameterised by its radius of curvature is used to smooth the ramp profile.

For a given choice of $S\mathscr{L}$ and α, a solution to the problem (2.6) subject to the boundary conditions (2.7) and the interaction condition (2.8) can be sought using the direct method presented in Broadley *et al.* (2023). This solves a discretised version of the system for all degrees of freedom simultaneously via Newton iteration. The only modification required by the additional term in the hypersonic interaction condition (2.8) is to include a second-order accurate central-difference representation of the pressure derivative.

2.2. *Linear three-dimensional disturbances*

Our goal is to assess the susceptibility of the nonlinear two-dimensional base flows described above to growth of three-dimensional linear disturbances. To do this, we seek perturbations of Görtler type, confined to the lower deck. The baseflow is steady, but we will include time-dependent terms for the disturbance, to capture the temporally growing modes discussed later in § 3.3 and the initial-value approach of § 3.4 below.

Following the incompressible formulation of Hall & Bennett (1986), we superimpose a linear three-dimensional perturbation $(\tilde{u},\, \tilde{v},\, \tilde{w},\, \tilde{p})$ to the above base flow of the form

$$\tilde{u} = \varepsilon M_\infty^{1/2} Re^{-1/8} \hat{h}_w^{1/2}\, \tilde{U}(X, Y, Z, T) + \cdots, \tag{2.11a}$$

$$\tilde{v} = \varepsilon M_\infty^{1/2} Re^{-3/8} \hat{h}_w^{1/2}\, \tilde{V}(X, Y, Z, T) + \cdots, \tag{2.11b}$$

$$\tilde{w} = \varepsilon M_\infty^{1/2} Re^{-3/8} \hat{h}_w^{1/2}\, \tilde{W}(X, Y, Z, T) + \cdots, \tag{2.11c}$$

$$\tilde{p} = \varepsilon \gamma M_\infty Re^{-6/8}\, \tilde{Q}(X, Y, Z, T) + \cdots, \tag{2.11d}$$

where $\varepsilon \ll 1$ is the amplitude of the disturbance and

$$\hat{z} = M_\infty^{3/2} Re^{-5/8} \hat{h}_w^{n+1/2}\, Z, \tag{2.11e}$$

$$\hat{t} = M_\infty Re^{-2/8} \hat{h}_w\, T\,. \tag{2.11f}$$

It is important to note that we have chosen a spanwise scale for the disturbance comparable to the depth of the viscous layer, as seen from (2.11*e*) and (2.5*b*). Other regimes are possible, as described by (for example) Hall (1982) and Timoshin (1990).

Substituting this expansion into the lower-deck equations we obtain the linearised triple-deck analogue of the Görtler equations

$$\tilde{U}_X + \tilde{V}_Y + \tilde{W}_Z = 0, \tag{2.12a}$$

$$\tilde{U}_T + \overline{U}_B \tilde{U}_X + \tilde{U}\,\overline{U}_{BX} + V_B \tilde{U}_Y + \tilde{V}\,\overline{U}_{BY} = \tilde{U}_{YY} + \tilde{U}_{ZZ}, \tag{2.12b}$$

$$\tilde{V}_T + \overline{U}_B \tilde{V}_X + \tilde{U}\, V_{BX} + \tilde{V}\, V_{BY} + V_B \tilde{V}_Y + 2\alpha F_{XX} \overline{U}_B \tilde{U} = -\tilde{Q}_Y + \tilde{V}_{YY} + \tilde{V}_{ZZ}, \tag{2.12c}$$

$$\tilde{W}_T + \overline{U}_B \tilde{W}_X + V_B \tilde{W}_Y = -\tilde{Q}_Z + \tilde{W}_{YY} + \tilde{W}_{ZZ}, \tag{2.12d}$$

where F_{XX} is the second derivative of the ramp shape and $\overline{U}_B = U_B(X, Y) + Y$. The governing equations are subject to periodicity in the spanwise (Z) coordinate, decay of the perturbation on leaving the lower deck ($Y \to \infty$) and when sufficiently far upstream ($X \to -\infty$). The perturbations are confined to the lower deck and decay as $Y \to \infty$ and there is no interaction condition.

To assess the response of the system to spanwise-varying upstream disturbances we allow for localised weak suction/blowing through the upstream plate surface, so the impermeability condition is replaced by

$$\tilde{V}(X, Y = 0, Z, T) = H(X, T) e^{i\beta Z} + \text{c.c.}, \tag{2.13}$$

where H is a function to be specified, $2\pi/\beta$ is the spanwise wavelength and c.c. indicates a complex conjugate. Note that one can equally perturb the flow using some other method, for example placing a spanwise varying roughness element upstream of the ramp as in Bassom & Hall (1994). We now seek solutions of the form

$$(\tilde{U}, \tilde{V}, \tilde{W}, \tilde{Q}) = (\hat{U}, \hat{V}, \hat{W}, \hat{Q}) e^{i\beta Z} + \text{c.c.}. \tag{2.14a}$$

Upon substitution into (2.12) this results in

$$\hat{U}_X + \hat{V}_Y + i\beta \hat{W} = 0, \tag{2.15a}$$

$$\hat{U}_T + \overline{U}_B \hat{U}_X + \hat{U}\overline{U}_{BX} + V_B \hat{U}_Y + \hat{V}\overline{U}_{BY} = \hat{U}_{YY} - \beta^2 \hat{U}, \tag{2.15b}$$

$$\hat{V}_T + \overline{U}_B \hat{V}_X + \hat{U} V_{BX} + \hat{V} V_{BY} + V_B \hat{V}_Y + 2\alpha F_{XX} \overline{U}_B \hat{U} = -\hat{Q}_Y + V_{YY} - \beta^2 \hat{V}, \tag{2.15c}$$

$$\hat{W}_T + \overline{U}_B \hat{W}_X + V_B \hat{W}_Y = -i\beta \hat{Q} + W_{YY} - \beta^2 \hat{W}, \tag{2.15d}$$

which is to be solved in conjunction with the boundary conditions

$$\hat{U} = \hat{W} = 0, \ \hat{V} = H(X, T) \quad \text{at} \quad Y = 0, \tag{2.16a}$$

$$\hat{U}, \hat{V}, \hat{W} \to 0 \quad \text{as} \quad Y \to \infty, \tag{2.16b}$$

$$\hat{U}, \hat{V}, \hat{W} \to 0 \quad \text{as} \quad X \to -\infty. \tag{2.16c}$$

For a given two-dimensional base flow $(\overline{U}_B, V_B)$ this problem can be solved directly at each time step using finite-differences in its current form. However, we choose to eliminate the perturbation pressure in a similar manner to Hall (1983). We cross-differentiate the transverse and spanwise momentum equations to eliminate $\hat{Q}$, and then we use the continuity equation to eliminate $\hat{W}$. This leaves a fourth-order differential equation for $\hat{V}$ as well as the unchanged streamwise momentum equation,

$$\hat{U}_T + \overline{U}_B \hat{U}_X + \hat{U}\overline{U}_{BX} + V_B \hat{U}_Y + \hat{V}\overline{U}_{BY} = \hat{U}_{YY} - \beta^2 \hat{U}, \tag{2.17a}$$

$$\begin{aligned} &\beta^2 \hat{V}_T - \hat{V}_{YYT} + \hat{V}_{YYYY} - V_B \hat{V}_{YYY} - \overline{U}_B \hat{V}_{XYY} - \left(2\beta^2 + V_{BY}\right)\hat{V}_{YY} \\ &\quad + \left(\overline{U}_{BXY} + \beta^2 V_B\right)\hat{V}_Y + \left(\overline{U}_{BYY} + \beta^2 \overline{U}_B\right)\hat{V}_X + \left(\overline{U}_{BXYY} + \beta^4 + \beta^2 V_{BY}\right)\hat{V} \\ &\quad + V_{BX}\hat{U}_{YY} + 2\overline{U}_{BX}\hat{U}_{XY} + 2\overline{U}_{BXY}\hat{U}_X + \left(\overline{U}_{BXXY} + \beta^2 V_{BX} + 2\alpha\beta^2 \overline{U}_B F_{XX}\right)\hat{U} = 0. \end{aligned} \tag{2.17b}$$

To obtain boundary conditions in terms of $\hat{U}$, $\hat{V}$ we evaluate the continuity equation at $Y=0$ and as $Y\to\infty$, giving

$$\hat{U}=\hat{V}_Y=0,\ \ \hat{V}=H(X,T)\quad \text{at}\quad Y=0, \tag{2.18a}$$

$$\hat{U},\hat{V},\hat{V}_Y\to 0,\quad \text{as}\quad Y\to\infty. \tag{2.18b}$$

For sufficiently small ramps the (2.17) are parabolic and unidirectional (i.e. $U_B\geqslant 0$ everywhere in the domain) and therefore a natural numerical procedure is to start at the furthest node upstream and march the solution downstream at each time step. However, for ramp angles larger than $\alpha\approx 1.6$ (for $S\mathscr{L}=0$) the base flow separates from the ramp surface for a finite region near the corner; Görtler vortices in an interactive separated flow have been considered before by Denier & Bassom (1996). The resulting upstream influence means that a simple parabolic marching algorithm does not suffice. One option is to solve the system using a zig–zag scheme similar to that of Cebeci (1979, 1986), or other windward differencing schemes, or to approach this problem with essentially the same direct method applied to the base flow. In each case the same non-uniform distribution of nodes applied to the baseflow is employed with second-order spatial differencing, together with a Crank–Nicolson method if time-marching is employed. Comparison of these approaches shows consistent results across ramp angles that induce both unidirectional and separated bidirectional base flows.

3. Results

3.1. *Steady base flows*

We begin in figure 2 by presenting some steady base flows at a representative (separated) ramp angle $\alpha=4.4$ and decreasing wall-cooling parameter $S\mathscr{L}$. We have already noted that for $S\mathscr{L}=0$ we recover the analogous supersonic problem, and the present numerical method produces results consistent with the literature (Broadley *et al.* 2023). In interpreting these figures we must remember that larger values of S are associated with wall cooling via a decreasing $\hat{h}_w$. This same $\hat{h}_w$ parameter affects the downstream scale via (2.5*a*), so as expected wall cooling reduces the spatial extent of the separation region.

Figure 2(*a*) shows the locus of points along which $\overline{U}_B=0$, therefore for each case, the flow is left-to-right above this line and right-to-left below it. In terms of figure 1 these baseflow states are entirely in the lower deck denoted as region 1.

For $S\mathscr{L}=0$ the flow is just approaching the point of secondary separation as seen in figure 2(*b*). We also see how wall cooling affects the separated region, particularly near the separation point. Increasingly negative values of $S\mathscr{L}$ are difficult to resolve owing to the rapid appearance of flow reversal over decreasing length scales near separation (e.g. $X\approx -10$ in figure 2*b*); this rapid change near the separation point is qualitatively consistent with the asymptotic ($S|\mathscr{L}|\gg 1$) theory of Kerimbekov *et al.* (1994). The asymptotic description provided by Kerimbekov *et al.* (1994) was later verified by the numerical results of Cassel *et al.* (1996) for large but finite values of $S|\mathscr{L}|$ and we have confirmed that we can reproduce the data in Cassel *et al.* (1996), figures 2–5 for $S\mathscr{L}<0$. For incipient separation, it is known from the strongly cooled asymptotic results that the ramp angle should increase in proportion to $|S\mathscr{L}|^{2/3}$.

In figure 2(*c*) we show the separation and reattachment points $X_{s,r}$ in both the wall-cooled $S\mathscr{L}=-5$ and $S\mathscr{L}=0$ cases. This level of wall cooling is sufficient to delay both incipient and secondary separation (denoted by $X_{1,2}$) to slightly larger ramp angles, and the scaled separation bubble size $l_B=X_r-X_s$ is reduced. The data points shown from

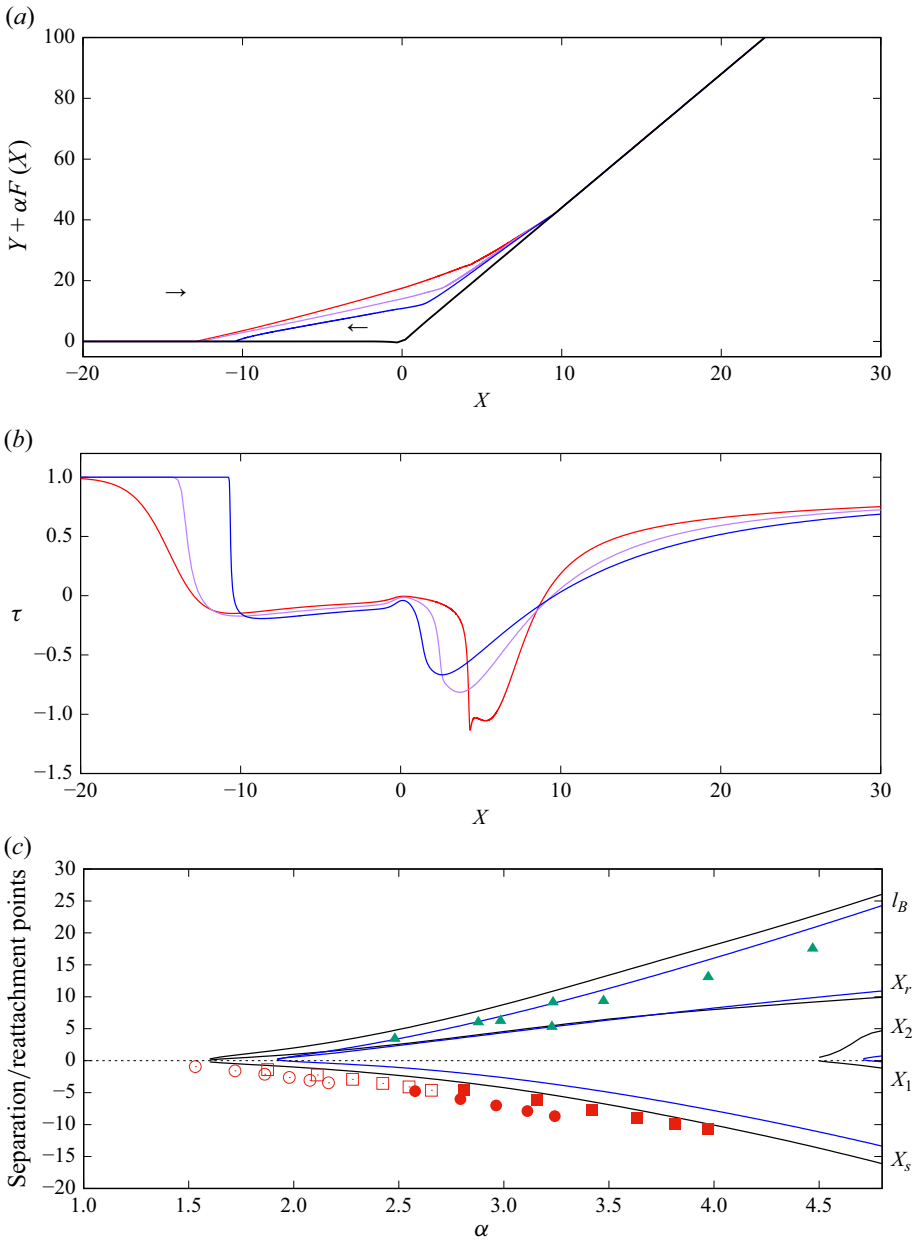

Figure 2. (*a*,*b*) Sample base flow state solutions to (2.6)–(2.8). (*a*) Contours of $\overline{U}_B \equiv Y + U_B(X, Y) = 0$, the arrows indicate left to right flow above this contour with reverse (right to left) flow below it; $\alpha = 4.4$, $S\mathscr{L} = 0$ (red), -2.5 (purple), -5 (blue). (*b*) Distribution of the shear $\tau \equiv 1 + U_{BY}(X, Y = 0)$ with $\tau < 0$ indicating the flow reversal; $\alpha = 4.4$, $S\mathscr{L} = 0$ (red), -2.5 (purple), -5 (blue). (*c*) Positions of separation X_s, reattachment X_r, secondary separation points $X_{1,2}$ and separation bubble length $l_B = X_r - X_s$ with $S\mathscr{L} = 0$ (black) and $S\mathscr{L} = -5$ (blue). Data points correspond to l_B obtained from (green upper) Gai & Khraibut (2019), their figure 17, and (red lower) X_s from Grisham *et al.* (2018), their figure 11.

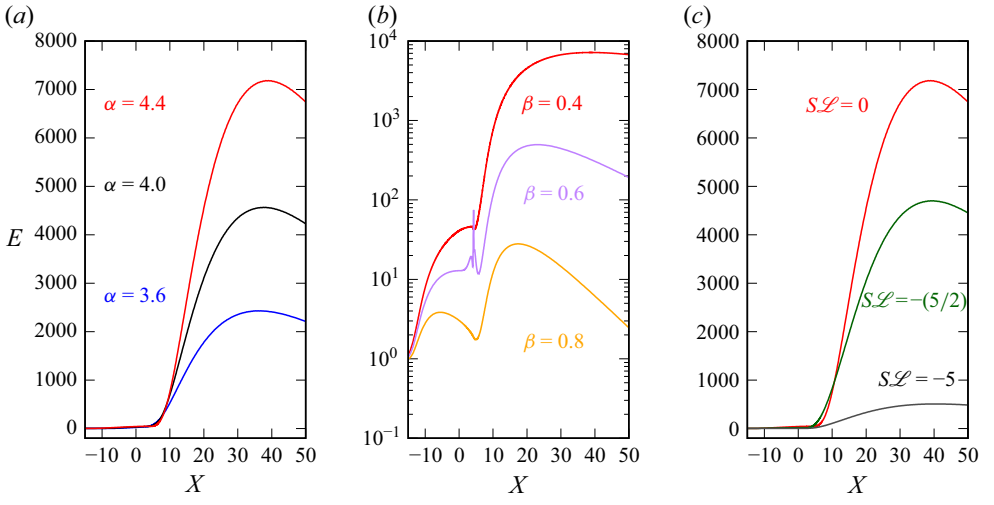

Figure 3. Development of the leading-order vortex kinetic energy $E(X)$ defined in (3.2) driven by upstream perturbation (3.1) with $X_0 = -40$: (*a*) varying ramp angle α with spanwise wavenumber $\beta = 0.4$ and $S\Omega = 0$; (*b*) varying spanwise wavenumber β with $\alpha = 4.4$ and $S\Omega = 0$; (*c*) varying wall cooling parameter $S\Omega$ with $\alpha = 4.4$ and $\beta = 0.4$.

Grisham, Dennis & Lu (2018) and Gai & Khraibut (2019) span Mach numbers up to 9.1, adiabatic wall conditions and Reynolds numbers in the range 10^{4-6}.

3.2. *Spatial instability to Görtler modes*

We first consider steady solutions of (2.17)–(2.18), to evaluate the spatial growth of steady perturbations introduced upstream. The disturbance is driven by a localised time-independent upstream wall injection in (2.18) of the form

$$\hat{V}(X, Y = 0, Z) = H(X) = e^{-\frac{1}{4}(X - X_0)^2}, \tag{3.1}$$

where $\tilde{V} = e^{i\beta Z}\hat{V} + \text{c.c.}$ is the transverse velocity perturbation and $X_0 < 0$ defines the upstream position of the disturbance. As a metric for the downstream growth we take a leading-order kinetic energy associated with the perturbation, which is dominated by the streamwise component $\tilde{U}$ in (2.11),

$$E(X) = \frac{1}{E_n}\int_0^\infty \hat{U}^2(X, Y)\,\mathrm{d}Y, \tag{3.2}$$

and E_n is a normalisation factor discussed below.

Having defined the metric $E(X)$ we then define the corresponding spatial growth rate in the usual manner

$$\sigma(X) = \frac{1}{2E}\frac{\mathrm{d}E}{\mathrm{d}X}. \tag{3.3}$$

Downstream of the disturbance generator there is a neutral point $X = X_n > X_0$ at which the disturbance first changes from stable ($\sigma < 0$) to unstable ($\sigma > 0$). We choose to normalise the energy measure (3.2) by choosing E_n such that $E(X_n) = 1$. In other words, the energy of the disturbance is set to unity at the first point of neutral growth on approaching the compression ramp corner. We can then compare the subsequent maximum amplification as the disturbance develops through the compression ramp.

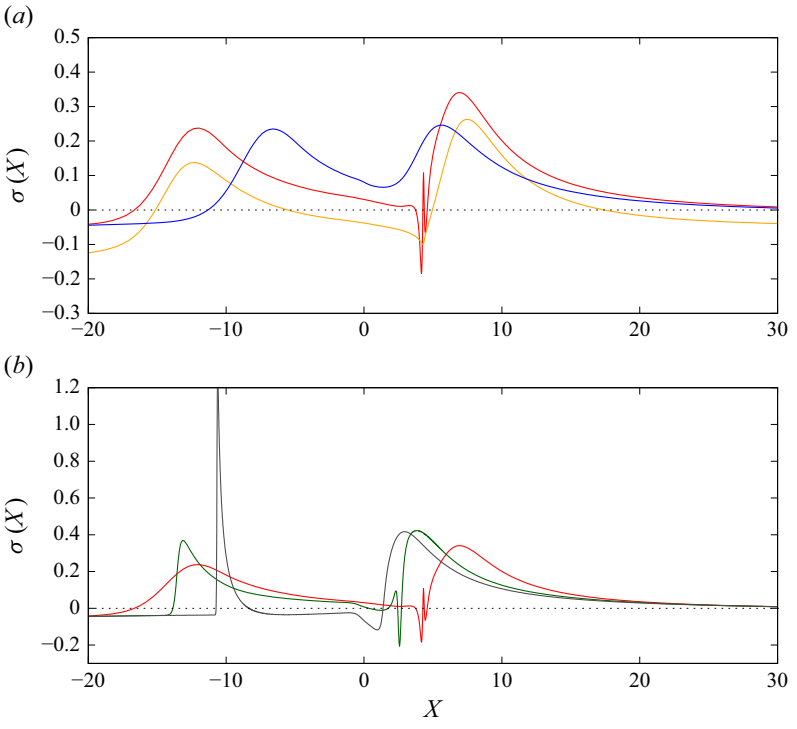

Figure 4. Growth rates computed from (3.3); the line colours correspond to the cases shown in figure 3. (*a*) Fixed $S\mathscr{L}=0$, with varying (red) $\alpha=4.4$, $\beta=0.4$, (blue) $\alpha=3.6$, $\beta=0.4$, (yellow). (*b*) Fixed $\alpha=4.4$, $\beta=0.4$, with varying wall cooling (red) $S\mathscr{L}=0$, (green) $S\mathscr{L}=-5/2$, (black) $S\mathscr{L}=-5$.

As this is a Görtler problem, the downstream evolution is strongly tied to the initial disturbance generator and its subsequent non-parallel development. Consistent with observations in DNS results, the results of figure 3 show that energy growth increases rapidly with ramp angle. Larger spanwise wavelengths have stronger peak growths, and the peak develops farther downstream from the corner. Wall cooling reduces the growth. There is an intermediate peak in E around $X=4$ shown in figure 3(*b*) for the case of $\beta=0.6$ – this is caused by a temporally neutral zero-frequency biglobal eigenmode, and we return to discuss this feature in § 3.3 below.

The spatial growth rates of figure 4 show two distinct peaks associated with the initial separation and subsequent reattachment regions of the baseflow. Wall cooling (figure 4*b*) leads to larger peak growth rates, see the green/black lines for $S\mathscr{L}=-5/2$ and -5 compared with the red line for $S\mathscr{L}=0$. However, whilst this peak growth rate increases, it typically applies over a shorter X length scale, leading to an overall smaller energy growth, as shown in figure 3(*c*). In interpreting these results one must remember that wall-cooling also changes the spanwise scale (2.11*e*), so in dimensional terms the upstream forcing has a different dimensional spanwise wavelength in the three cases of figure 3(*c*), even though all three have the same scaled dimensionless wavenumber of $\beta=0.4$.

In figure 5 we show the downstream evolution of streamwise and spanwise velocity perturbations that are initiated upstream at $X=X_0=-40$, with wall cooling $S\mathscr{L}=-2.5$ and a spanwise wavenumber of $\beta=0.4$. Downstream of the forcing location on the 'horizontal' boundary (ahead of the ramp) the perturbation decays and is largely invisible on the scale of figure 5. However, post separation there is strong amplification of both the spanwise velocity component and the streamwise velocity component such that a clear

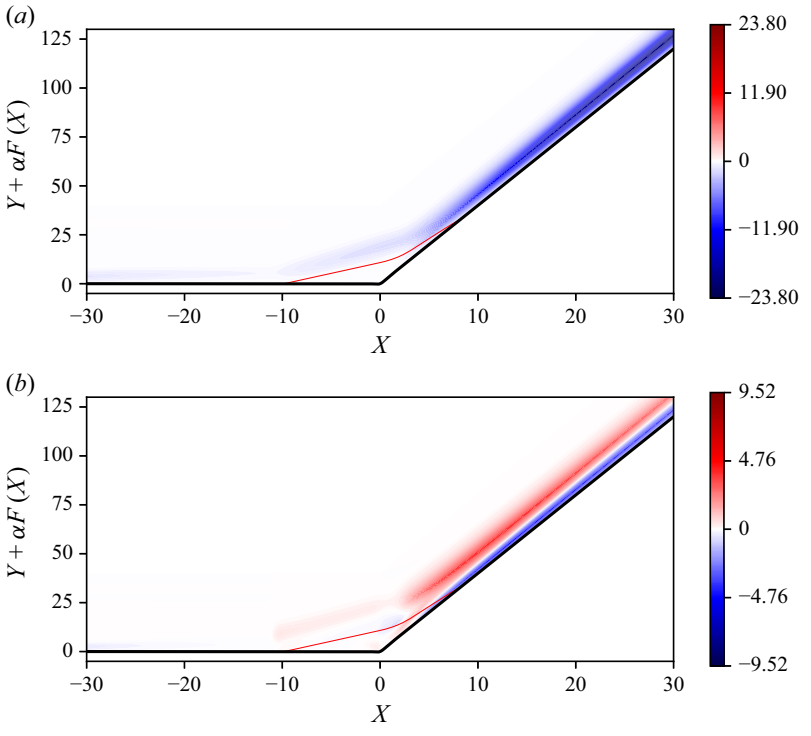

Figure 5. Evolution of the linearised perturbation velocity components: (*a*) streamwise $\hat{U}(X, Y)$; (*b*) spanwise $\hat{W}(X, Y)$. The disturbance is generated at $X = X_0 = -40$ with ramp angle $\alpha = 4.0$, spanwise wavenumber $\beta = 0.4$ and wall cooling $S\mathscr{L} = -2.5$. The red line delineates the region of reverse flow in the underlying two-dimensional base flow.

streak/vortex is visible adjacent to the deflected ramp surface. Over a larger X scale than that shown in figure 5 the response again decays farther downstream in line with the results of figures 3 and 4.

When viewed in the cross-sectional plane, we can see from figure 6(*a*) that in the separated part of the flow, the disturbance is displaced above the reverse flow region. The response is strongest in the neighbourhood of the reattachment point, where a now obvious downstream streak/vortex is observed in figure 6(*b*), now adjacent to the ramp surface post reattachment. Sufficiently far downstream of reattachment the linear response is one of decay, with $\sigma < 0$ as seen in figure 4.

3.3. *Biglobal three-dimensional modes*

Spanwise periodic structures can also develop as a temporal instability without any explicit forcing via the upstream flow boundary conditions (i.e. $H \equiv 0$). In the literature, these are presented as 'intrinsic' instabilities, and therefore we now address the possibility of temporally unstable, biglobal, spanwise periodic, eigenmodes to the lower-deck of the triple-deck description.

A biglobal eigenvalue problem can be formulated from (2.17) (without upstream forcing, so $H \equiv 0$) by seeking solutions of the form

$$(\tilde{U}, \tilde{V}) = e^{\hat{s}T}\, e^{i\beta Z}\, (\hat{U}, \hat{V}), \tag{3.4}$$

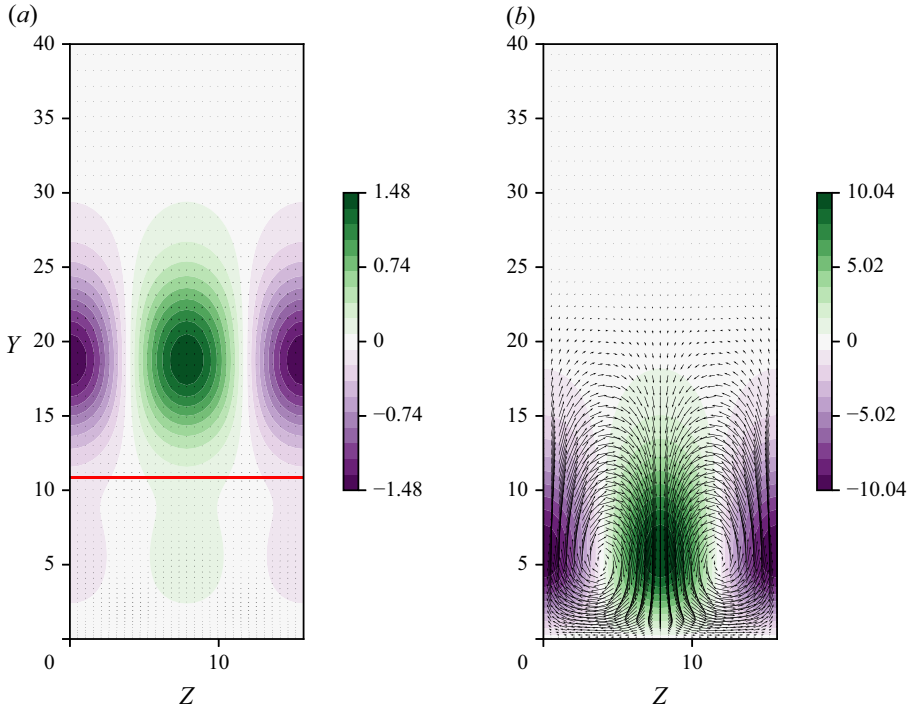

Figure 6. Cross sections in the Y–Z plane for a steady disturbance generated at $X = X_0 = -40$ with ramp angle $\alpha = 4.0$, spanwise wavenumber $\beta = 0.4$ and wall cooling $S\mathscr{L} = -2.5$. Contours show the streamwise velocity perturbation $\tilde{U}$, whilst the vector field is the associated in-plane $(\tilde{U},\tilde{W})$ velocity field at (a) $X = 0$, the red line separates regions of $\overline{U}_B < 0$ (below) to $\overline{U}_B > 0$ (above) and (b) $X = 10$. The vector field is scaled the same way in both (a) and (b).

where β (real) is to be specified, $\hat{s}$ is a complex eigenvalue associated with the temporal growth-rate/frequency and the eigenfunctions $(\hat{U}, \hat{V})$ depend on both X and Y. Given a solution to this problem, the corresponding $\tilde{W}$ and $\tilde{Q}$ can be determined by back substitution into (2.15).

In figure 7(a) we show the loci of ramp-angle α and spanwise wavelength $2\pi/\beta$ along which a neutral biglobal eigenmode is achieved $(\hat{s}_r = 0)$ for two representative cases $S\mathscr{L} = 0$ and $S\mathscr{L} = -5/2$ (wall cooled). Along these boundaries the imaginary part of $\hat{s}$ also remains zero and at least one unstable eigenmode exists for ramp angles above these neutral curves. The existence of such modes explains the localised spike near $X \approx 4$ in figure 3(b) when $\beta = 0.6$ and $S\mathscr{L} = 0$; the parameter choices in that figure are very close to neutral for a biglobal mode and are represented by the left-most data point in figure 7.

In figure 7(b) we overlay the same neutral curves with published data from the NSE computations of Li & Hao (2023) in red and Hao *et al.* (2021) in yellow. The boundary α_{inc} is the scaled critical ramp angle for incipient separation, α_{sec} is the angle for secondary separation, and α_{GSA} is the boundary obtained for global stability via computation of the linearised NSE (LNSE). The computational data shown in red is for adiabatic wall conditions. For a cooled wall, the global stability boundary of Hao *et al.* (2021) (figure 14 in that work) spans the yellow region for T_w/T_0 in the range of 0.18–0.86. For comparison, the green lines for α_{inc} and α_{sec} are obtained from the triple-deck baseflow states used herein.

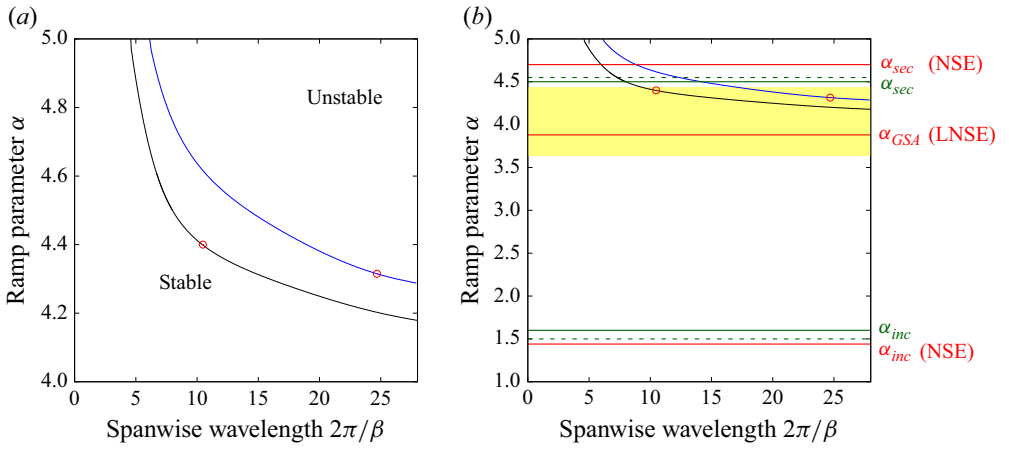

Figure 7. (*a*) Loci of neutral ($\hat{s}_r = 0$) biglobal eigenmodes in the case $S\mathscr{L} = 0$ (lower, black) and a cooled-wall case $S\mathscr{L} = -2.5$ (upper, blue). The eigenfunctions associated with the two red data points are shown in figure 8(*a*,*b*). (*b*) The same neutral curves overlaid with critical ramp parameters for incipient separation α_{inc}, secondary separation α_{sec} and first global instability α_{GSA} without cooling, as presented in the LNSE results of Li & Hao (2023), their figure 25 (red). The yellow region indicates the range of α_{GSA} obtained in Hao *et al.* (2021), their figure 14 under wall cooling. The corresponding separation values for the triple-deck formulation are shown in solid green ($S\mathscr{L} = 0$) and dashed green ($S\mathscr{L} = -2.5$).

The analysis of (Hao *et al.* 2021) suggested that global instability is 'closely linked' with secondary separation with unstable eigenmodes occurring 'immediately prior' to this. The neutral curves of figure 7(*a*,*b*) exist at ramp angles both below and above the critical value required for secondary separation. However, the biglobal modes occur first at large (scaled) wavelength and this point is at a slightly smaller ramp angle than that associated with secondary separation.

Figure 8(*a*,*b*) show the spanwise velocity $\hat{W}(X, Y)$ of the neutral eigenmode at the two data points located on the neutral curves shown in figure 7(*a*). Also shown are the streamlines associated with the separation region in the base flow. We see that in all cases the eigenmode is localised around the 'eye' of this recirculating flow. The analysis of Hao *et al.* (2021) shows that this location dominates disturbance energy production in an analysis of eigenmodes obtained from the LNSE system.

By contrast, figure 8(*c*) shows an unstable eigenmode for $S\mathscr{L} = 0$, but at a ramp angle α and wavenumber β equal to those of figure 8(*b*). The structure remains similar to the neutrally stable case of figure 8(*a*) at smaller wavelength. Qualitative comparison of figure 8 with those of Hao *et al.* (2021), their figures 10 and 11 (which it should be noted are at larger wavelengths than considered here) show that while both sets remain confined to the separation bubble, in the LNSE calculations the streamwise extent is longer, encompassing most of the length of the separated region. However, in the study of Sidarth *et al.* (2017) (who performed calculations at a higher Reynolds number), their figures 11, 12, 15 and 17 show modes with similar qualitative behaviour as those observed in the present case, with most of the spanwise velocity disturbance localised to the eye of the bubble.

Although our chosen vortex wavelength scale (2.11*e*) captures the left-hand branch of the neutral curve shown in figure 7, it cannot capture the larger scales required for a peak growth rate; the wavelengths of eigenmodes shown in Hao *et al.* (2021) are not of this scale. It should be further noted that wall cooling in the results of Hao *et al.* (2021) leads

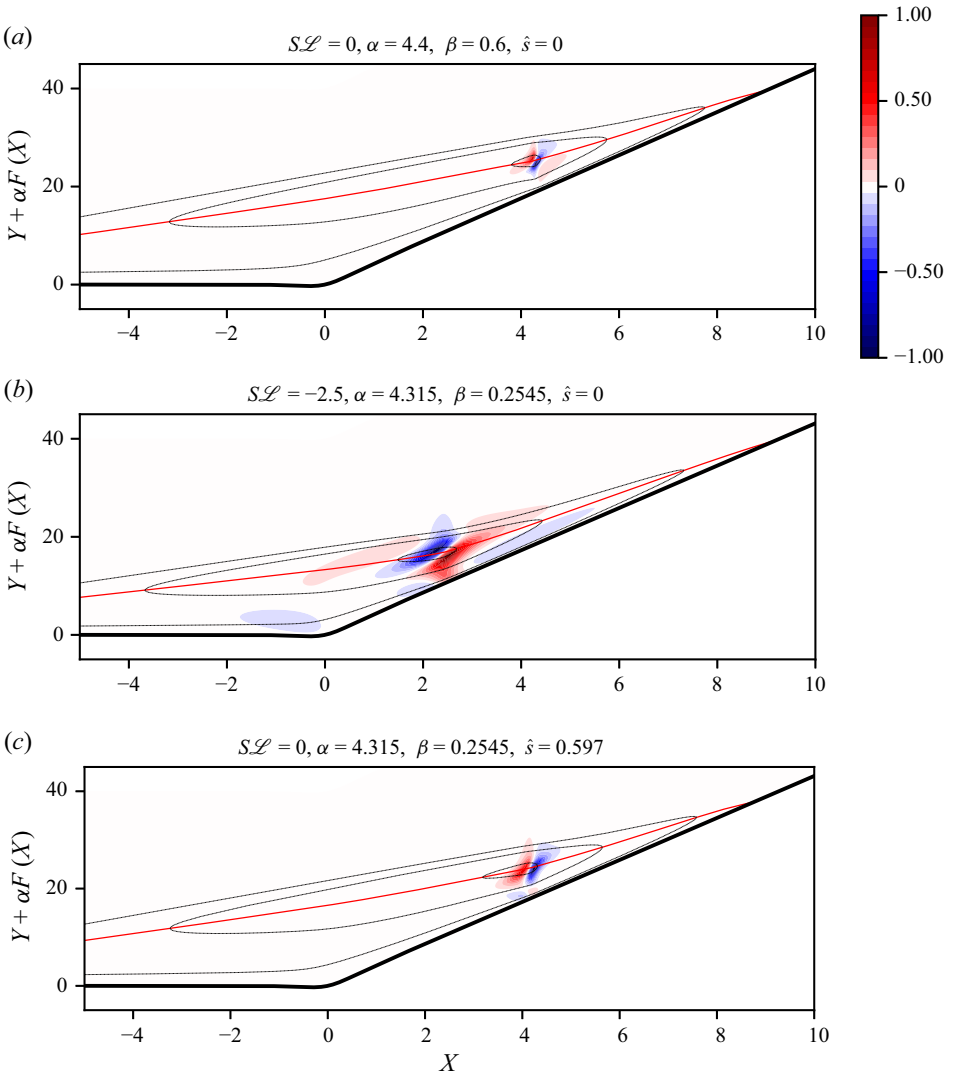

Figure 8. The biglobal eigenmode showing contours of spanwise velocity $\hat{W}$ normalised to have a peak absolute value of unity: panels (*a*) and (*b*) are neutral modes corresponding to the data points in figure 7, panel (*c*) is an unstable mode. The red line in each figure indicates the points of zero streamwise velocity in the base flow, $\overline{U}_B(X, Y) = 0$, with reverse flow below this level. The black lines indicate the streamlines of the recirculation region, with 95 %, 50 % and 5 % of the peak negative stream function value. The colour bar applies to all three figures.

to a lower ramp angle for instability over these larger wavelengths, whereas figure 7(*a*) shows that in the asymptotic problem for smaller wavelengths it is stabilising.

Figures 9(*a*) and 9(*b*) show profiles of eigenmode velocities alongside the baseflow velocity at $X = X_c$ for cases in figures 8(*c*) and 8(*b*), respectively. The position X_c is chosen to be the downstream position of the 'eye' of the recirculation in the separated flow. In these cross-sections, the eigenmode velocities attain their maximum amplitudes in near to the 'eye' (where there is a stagnation point in the leading-order base flow solution).

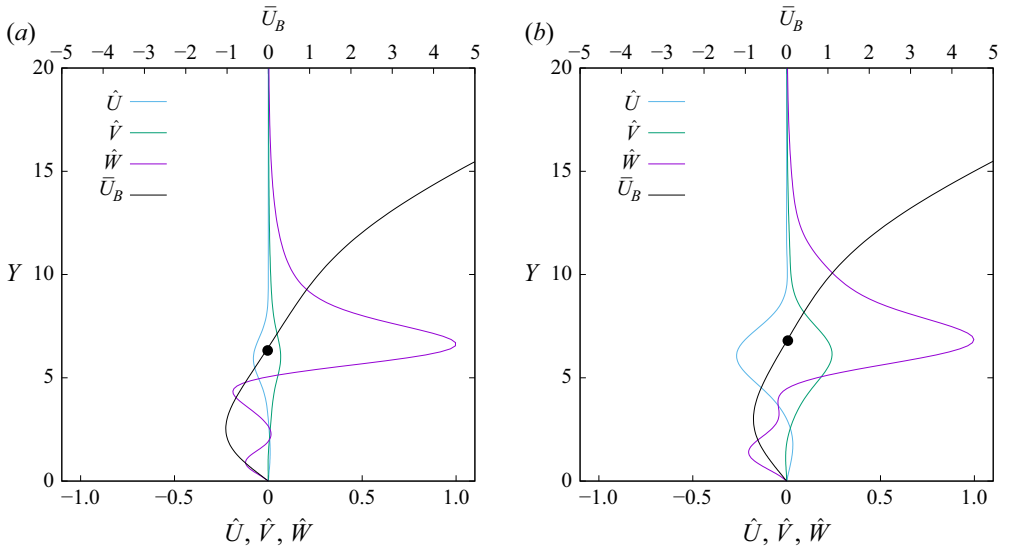

Figure 9. Profiles of the baseflow $\overline{U}_B$ and eigenmode velocities $(\hat{U}, \hat{V}, \hat{W})$ at $X = X_c$ for $\alpha = 4.315$, $\beta = 0.2545$ for (*a*) $S\mathscr{L} = 0$, $X_c = 4.07$ and (*b*) $S\mathscr{L} = -2.5$, $X_c = 2.26$. The chosen positions $X = X_c$ correspond to the 'eye' of the baseflow recirculation in each case (indicated by the data point), as seen in figure 8(*b*,*c*). The eigenmode is normalised to have a peak $\hat{W}$ velocity of unity at X_c.

3.4. *Initial-value calculations*

As a check that the results of the biglobal eigenvalue problem studied above are valid and capture the most unstable mode, we can also solve a suitable initial-value problem for the Görtler (2.17). To reproduce the results of § 3.2 we start from an unperturbed state, then increase the amplitude of forcing upstream to a steady value as time increases. Similarly for the eigenmodes obtained in § 3.3 we can perform a similar computation, but the forcing is only applied transiently. Here we make a direct comparison only for the eigenmodes.

To obtain a temporal growth rate for the response we choose a metric to track through time. To this end, we use the perturbation to the wall shear stress $\hat{\tau}$:

$$\hat{\tau}(X, 0, T) = \hat{U}_Y(X, 0, T). \tag{3.5}$$

It takes some time for the initial perturbation to be convected to the separated region, where growth will begin to occur for sufficiently inclined ramps. To detect this growth we will examine the maximum value of $|\hat{\tau}|$ over all downstream positions, then once exponential growth is obtained, we can compare the growth rate (and flow field) with the predictions of § 3.3.

We set the ramp angle to $\alpha = 4.4$ and compute the response for two base flows: (i) $S\mathscr{L} = 0$, (ii) $S\mathscr{L} = -2.5$ for disturbances of wavenumber for $\beta = 0.5, 0.3$, respectively. Figures 10(*a*) and 10(*b*) are semilogarithmic plots of the maximum of $\hat{\tau}$ across the streamwise domain against time. In both cases there is an initial growth in the maximum amplitude of $\hat{\tau}$ that is associated with the transient forcing. Following this, once the disturbance is present in the separated region, we achieve an exponential response in the time-marched results. The dotted lines in figure 10 have gradients of 0.41 and 0.0936, respectively.

Comparing these growth rates obtained from the initial-value problem (denoted $\hat{s}_{IVP}$) and the biglobal eigenproblem (denoted $\hat{s}_{BG}$) we have

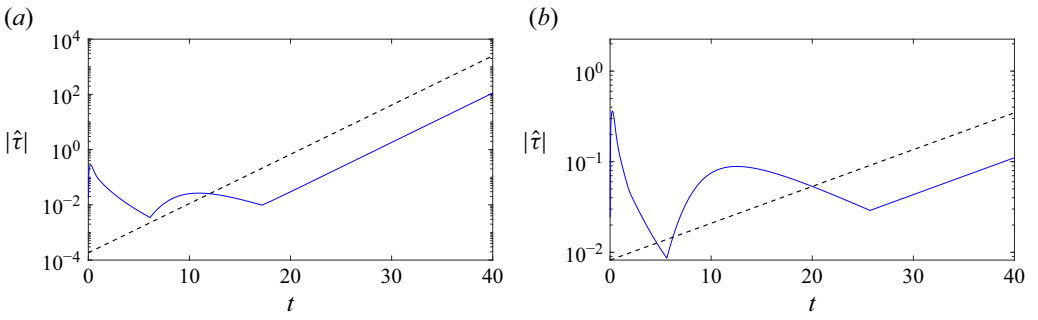

Figure 10. The evolution of the streamwise maximum of wall-shear contribution $|\hat{\tau}|$ with time for (*a*) $\alpha = 4.4$, $S\mathscr{L} = 0$, $\beta = 0.5$ and (*b*) $\alpha = 4.4$, $S\mathscr{L} = -2.5$, $\beta = 0.3$ as calculated from the initial-value problem (blue lines). Black dotted line corresponds to estimated growth rates of (*a*) $Re\{\hat{s}\} = 0.41$, (*b*) $Re\{\hat{s}\} = 0.0936$.

$$Re\big(\hat{s}_{IVP}\big) = 0.41, \qquad Re\big(\hat{s}_{BG}\big) = 0.40, \tag{3.6}$$

for $S\mathscr{L} = 0$, $\beta = 0.5$. Similarly, for $S\mathscr{L} = -2.5$, $\beta = 0.3$ the comparison is

$$Re\{\hat{s}_{IVP}\} = 0.0936, \qquad Re\big(\hat{s}_{BG}\big) = 0.0906, \tag{3.7}$$

respectively. Comparisons of the flow field obtained for large times in the time-marched results also compare well with the eigenmodes obtained directly. This gives us some confidence that the 'exchange of stability' predicted in figure 7 is realised in the initial-value computation of (2.17).

4. Discussion

We have demonstrated that the large Reynolds/Mach-number asymptotic structure allows for spatial amplification of Görtler perturbations and global instabilities localised in the separation region. For modest ramp angles the separation region is confined to the lower-deck scale, and a key point is that this lower layer remains thin relative to the oncoming boundary layer. As a consequence, to leading order there are no density/temperature variations, ruling out baroclinic mechanisms of growth. Of course this does not say that such mechanisms cannot be important on other scales (Dwivedi *et al.* 2019). Nevertheless the spatial growth of upstream steady disturbances near separation and reattachment (figure 4), displacement of these disturbances above the separation region (figure 5), and localisation of temporal biglobal eigenmodes in the separation region (figure 8) are features that are also found in finite-Reynolds number computational results.

Our study is restricted to Görtler vortices of spanwise wavelengths comparable to the transverse lower-deck scale, which is the scale that describes the depth of the separation bubble. The open neutral curve of figure 7(*a*) and the increasing energy growth in figure 3(*b*) suggest that the most-dangerous wavelength of biglobal modes and maximum energy growth is achieved for larger wavelength disturbances. For spanwise wavelengths that are large compared with the transverse/separation-depth scale (2.17) are no longer appropriate. The different regimes of the Görtler problem are well known and described in Hall (1982), Timoshin (1990) and schematically in figure 2 of Hall (2021).

The role of a larger scaled vortex wavelength and nonlinear interactions of the disturbance remain topics of ongoing work. The approach of Ruban & Kravtsova (2013) has examined three-dimensional flow induced by an isolated roughness element in hypersonic flow, where the spanwise scale is large compared with the transverse scale of separation, but remains comparable to its downstream scale. The nonlinear generation

of additional harmonics in (2.11) can be included to obtain nonlinear states. Such states could then also be assessed for a secondary instability by a local short-wave analysis in the manner of (for example) Hall (1988) and Hall & Horseman (1991).

Funding. H.B. acknowledges the funding of the EPSRC.

Declaration of interests. The authors report no conflict of interest.

References

Bassom, A.P. & Hall, P. 1994 The receptivity problem for $O(1)$ wavelength Görtler vortices. *Proc. R. Soc. A* **446**, 499–516.

Broadley, H.M., Hewitt, R.E. & Gajjar, J.S.B. 2023 High-frequency instabilities in supersonic compression-ramp flow. *J. Fluid Mech.* **968**, A5-1–A5-22.

Brown, S.N., Cheng, H.K. & Lee, C.J. 1990 Inviscid-viscous interaction on triple-deck scales in a hypersonic flow with strong wall cooling. *J. Fluid Mech.* **220**, 309–337.

Cao, S., Hao, J., Guo, P., Wen, C.-Y. & Klioutchnikov, I. 2023 Stability of hypersonic flow over a curved compression ramp. *J. Fluid. Mech.* **957**, A8-1–A8-22.

Cao, S., Klioutchnikov, I. & Olivier, H. 2019 Görtler vortices in hypersonic flow on compression ramps. *AIAA J.* **57**, 3874–3884.

Cassel, K., Ruban, A.I. & Walker, J.D.A. 1995 An instability in supersonic boundary-layer flow over a compression ramp. *J. Fluid Mech.* **300**, 265–286.

Cassel, K.W., Ruban, A.I. & Walker, J.D.A. 1996 The influence of wall cooling on hypersonic boundary-layer separation and stability. *J. Fluid Mech.* **321**, 189–216.

Cebeci, T. 1979 The laminar boundary layer on a circular cylinder started impulsively from a rest. *J. Comput. Phys.* **31**, 153–172.

Cebeci, T. 1986 Unsteady boundary layers with an intelligent numerical scheme. *J. Fluid Mech.* **163**, 129–140.

Chuvakhov, P.V., Borovoy, V.Y., Egorov, I.V., Radchenko, V.N., Olivier, H. & Roghelia, A. 2017 Effect of small bluntness on formation of Görtler vortices in a supersonic compression corner flow. *J. Appl. Mech. Tech. Phys.* **58**, 975–989.

Denier, J.P. & Bassom, A.P. 1996 The existence of Görtler vortices in separated boundary layers. *Stud. Appl. Math.* **96**, 247–271.

Dwivedi, A., Sidarth, G.S., Nichols, J.W., Candler, G.V. & Jovanović, M.R. 2019 Reattachment streaks in hypersonic compression ramp flow: an input–output analysis. *J. Fluid Mech.* **880**, 113–135.

Fletcher, A.J.P., Ruban, A.I. & Walker, J.D.A. 2004 Instabilities in supersonic compression ramp flow. *J. Fluid Mech.* **517**, 309–330.

Gai, S.L. & Khraibut, A. 2019 Hypersonic compression corner flow with large separated regions. *J. Fluid Mech.* **877**, 471–494.

Grasso, F. & Marini, M. 1995 TVD multigrid solutions of three-dimensional viscous hypersonic flows. In *33rd Aerospace Sciences Meeting and Exhibit*, p. 470.

Grisham, J.R., Dennis, B.H. & Lu, F.K. 2018 Incipient separation in laminar ramp-induced shock-wave/boundary-layer interactions. *AIAA J.* **56** (2), 524–531.

Hall, P. 1982 Taylor–Görtler vortices in fully developed or boundary-layer flows: linear theory. *J. Fluid Mech.* **124**, 475–494.

Hall, P. 1983 The linear development of Görtler vortices in growing boundary layers. *J. Fluid Mech.* **130**, 41–58.

Hall, P. 1988 The nonlinear development of Görtler vortices in growing boundary layers. *J. Fluid Mech.* **193**, 243–266.

Hall, P. 2021 Long wavelength streamwise vortices caused by wall curvature or roughness. *J. Eng. Math.* **128** (1), 2.

Hall, P. & Bennett, J. 1986 Taylor–Görtler instabilities of Tollmien–Schlichting waves and other flows governed by the interactive boundary-layer equations. *J. Fluid Mech.* **171**, 441–457.

Hall, P. & Horseman, N.J. 1991 The linear inviscid secondary instability of longitudinal vortex structures in boundary layers. *J. Fluid Mech.* **232**, 357–375.

Hao, J., Cao, S., Wen, C.-Y. & Olivier, H. 2021 Occurrence of global instability in hypersonic compression corner flow. *J. Fluid. Mech.* **919**, A4-1–A4-20.

Inger, G.R. 1977 On the curvature of compressible boundary layer flows near separation. *Z. Angew. Math. Physik ZAMP* **28** (6), 1027–1035.

Kerimbekov, R.M., Ruban, A.I. & Walker, J.D.A. 1994 Hypersonic boundary-layer separation on a cold wall. *J. Fluid Mech.* **274**, 163–195.

KOROLEV, G.L., GAJJAR, J.S.B. & RUBAN, A.I. 2002 Once again on the supersonic flow separation near a corner. *J. Fluid Mech.* **463**, 173–199.
LI, C. & HAO, J. 2023 Global stability of supersonic flow over a hollow cylinder/flare. *J. Fluid. Mech.* **975**, A40-1–A40-35.
LOGUE, R.P., GAJJAR, J.S.B. & RUBAN, A.I. 2014 Instability of supersonic compression ramp flow. *Phil. Trans. R. Soc. A* **372**, 202130342.
NAVARRO-MARTINEZ, S. & TUTTY, O.R. 2005 Numerical simulation of Görtler vortices in hypersonic compression ramps. *Comput. Fluids* **34**, 225–247.
NEILAND, V.Y. 1969 Theory of laminar boundary layer separation in supersonic flow. *Izv. Akad. Nauk SSSR, Mech. Zhidk, Gaza* **4**, 53–57.
NEILAND, V.Y. 1973 Peculiarities of boundary-layer separation on a cooled body and its interaction with a hypersonic flow. *Izv. Akad. Nauk SSSR, Mech. Zhidk, Gaza* **6**, 99–109.
RIZZETTA, D.P., BURGGRAF, O.R. & JENSEN, R. 1979 Triple-deck solutions for viscous supersonic and hypersonic flow past corners. *J. Fluid Mech.* **89**, 535–552.
RUBAN, A.I. 1978 Numerical solution of the local asymptotic problem of the unsteady separation of a laminar boundary layer in a supersonic flow. *USSR Comput. Maths. Math. Phys.* **18**, 175–187.
RUBAN, A.I. 2017 *Fluid Dynamics: Part 3, Boundary Layers*. Oxford University Press.
RUBAN, A.I. & KRAVTSOVA, M.A. 2013 Generation of steady longitudinal vortices in hypersonic boundary layer. *J. Fluid Mech.* **729**, 702–731.
SIDARTH, G.S., DWIVEDI, A., CANDLER, G.V. & NICHOLS, J.W. 2017 Global linear stability analysis of high speed flows on compression ramps. In *47th AIAA Fluids Dynamics Conference*, p. 3455. AIAA (American Institution of Aeronautics and Astronautics).
SIDARTH, G.S., DWIVEDI, A., CANDLER, G.V. & NICHOLS, J.W. 2018 Onset of three-dimensionality in supersonic flow over a slender double wedge. *Phys. Rev. Fluids* **3**, 093901-1–093901-29.
SIMEONIDES, G. & HAASE, W. 1995 Experimental and computational investigations of hypersonic flow about compression ramps. *J. Fluid Mech.* **283**, 17–42.
SMITH, F.T. 1976*a* Flow through constricted or dil*a*ted pipes and channels: part 1. *Q. J. Mechan. Appl. Math.* **29** (3), 343–364.
SMITH, F.T. 1976*b* Flow through constricted or dilated pipes and channels: part 2. *Q. J. Mechan. Appl. Math.* **29** (3), 365–376.
SMITH, F.T. 1979*a* Nonlinear stability of boundary layers for disturbances of various sizes. *Proc. R. Soc. London* **368**, 573–589.
SMITH, FRANK THOMAS 1979*b* On the non-parallel flow stability of the blasius boundary layer. *Proc. R. Soc. London A Math. Phys. Sci.* **366**, (1724), 91–109.
SMITH, F.T. 1989 On the first-mode instability in subsonic, supersonic or hypersonic boundary layers. *J. Fluid Mech.* **198**, 127–153.
SMITH, F.T. & KHORRAMI, A. 1991 The interactive breakdown in supersonic ramp flow. *J. Fluid Mech.* **224**, 197–215.
STEWARTSON, K. & WILLIAMS, P.G. 1969 Self-induced separation. *Proc. R. Soc. London A* **312**, 181–206.
TERENT'EV, E.D. 1981 Linear problem for a vibrator in subsonic boundary layer. *Prikl. Mat. Mech.* **45**, 1049–1055.
TIMOSHIN, S.N. 1990 Asymptotic analysis of a spatially unstable Görtler vortex spectrum. *Fluid Dyn.* **25** (1), 25–33.
UY, K.C.K., HAO, J. & WEN, C.-Y. 2023 Global and local analyses of the Görtler instability in hypersonic flow. *Phys. Fluids* **35** (6), 064111-1–064111-16.
XU, D., RICCO, P. & DUAN, L. 2024 Görtler instability and transition in compressible flows. *AIAA J.* **62** (2), 489–517.